

## Demonstration of Acoustic Higher-Order Topological Stiefel-Whitney Semimetal

Xiao Xiang,<sup>1</sup> Yu-Gui Peng,<sup>1,\*</sup> Feng Gao,<sup>1</sup> Xiaoxiao Wu,<sup>2,3</sup> Peng Wu,<sup>1</sup>  
Zhaoxian Chen,<sup>4</sup> Xiang Ni,<sup>5,†</sup> and Xue-Feng Zhu<sup>1,‡</sup>

<sup>1</sup>*School of Physics and Innovation Institute, Huazhong University of Science and Technology, Wuhan 430074, China*

<sup>2</sup>*Quantum Science and Technology Center and Advanced Materials Thrust,*

*The Hong Kong University of Science and Technology (Guangzhou), Nansha, Guangzhou 511400, Guangdong, China*

<sup>3</sup>*Department of Physics, The Hong Kong University of Science and Technology, Clear Water Bay, Kowloon, Hong Kong, China*

<sup>4</sup>*College of Engineering and Applied Sciences, Collaborative Innovation Center of Advanced Microstructures, and National Laboratory of Solid State Microstructures, Nanjing University, Nanjing 210023, China*

<sup>5</sup>*School of Physics, Central South University, Changsha 410083, China*



(Received 20 May 2023; accepted 12 April 2024; published 10 May 2024)

The higher-order topological phases have attracted intense attention in the past years, which reveals various intriguing topological properties. Meanwhile, the enrichment of group symmetries with projective symmetry algebras redefines the fundamentals of topological matter and makes Stiefel-Whitney (SW) classes in classical wave systems possible. Here, we report the experimental realization of higher-order topological nodal loop semimetal in an acoustic system and obtain the inherent SW topological invariants. In stark contrast to higher-order topological semimetals relating to complex vector bundles, the hinge and surface states in the SW topological phase are protected by two distinctive SW topological charges relevant to real vector bundles. Our findings push forward the studies of SW class topology in classical wave systems, which also show possibilities in robust high- $Q$ -resonance-based sensing and energy harvesting.

DOI: [10.1103/PhysRevLett.132.197202](https://doi.org/10.1103/PhysRevLett.132.197202)

The everlasting goal of condensed matter physics is to search for new exotic matter, such as topological insulators and semimetals [1–3]. The topological insulator is featured with backscattering immune electron transport on matter surfaces [4,5]. Encouraged by the discovery of exotic topological phases in quantum materials, researchers have transposed the topological concept into classical systems and further explored novel topological phases [4–12]. In the past years, the higher-order topological phases have gradually gathered attention due to the emergence of more abundant topological effects [13–19]. For example, a  $d$ -dimensional  $n$ th-order topological phase can support  $(d - n)$  dimensional boundary states [20–24]. With unremitting efforts, 3D higher-order topological insulators and topological semimetals have been demonstrated in various classical systems [25–30]. Almost all previous higher-order topological semimetals have broken parity-time ( $PT$ ) symmetry and thus are described by complex vector bundles in the Hilbert space [23,24,27–30]. However, for the classical wave systems with  $PT$  symmetry, the Bloch wave function can be real; in such cases, topological classification rooted in complex space is no longer applicable [31]. A natural question arises as to whether there exists a topological class that can characterize the topological phase of real-valued higher-order topological semimetals.

Recently, Stiefel-Whitney (SW) invariants have been extended into condensed matter physics [31–35]. In

mathematics, there are four different types of characteristic classes: Chern classes, SW classes, Pontryagin classes, and Euler classes [36], where the SW classes are as important as the Chern classes. In condensed matter physics, the Chern classes have been widely explored, whereas the SW classes have yet not been well established. Benefiting from the algebraic relations of symmetry that can be projectively represented [37–40], theoretical models of higher-order topological Stiefel-Whitney semimetal (HOTSWS) were proposed [33–35]. However, the HOTSWS are yet to be implemented in experiments, which impedes the development of SW class-related topological physics and their applications.

In this Letter, we report the realization of acoustic HOTSWS by constructing  $\pi$  flux to obtain  $\mathbf{Z}_2$  artificial gauge field, which is a 3D second-order topological nodal loop semimetal. The acoustic HOTSWS is characterized by two SW topological charges of different orders (viz.,  $w_1$  and  $w_2$ ) and can have real wave functions under the  $PT$  symmetry, fundamentally differing from the Chern-class topological matter. In particular, the second-order topological invariant  $w_2$  is unique and carried by the nodal loops of HOTSWS, which we quantitatively verify in a realistic acoustic system with continuous wave distributions. Furthermore, the nodal loops are stable and never annihilate via the energy band reinversion under symmetry protection. We further experimentally demonstrate that the topological hinge states and surface states coexisted around the same

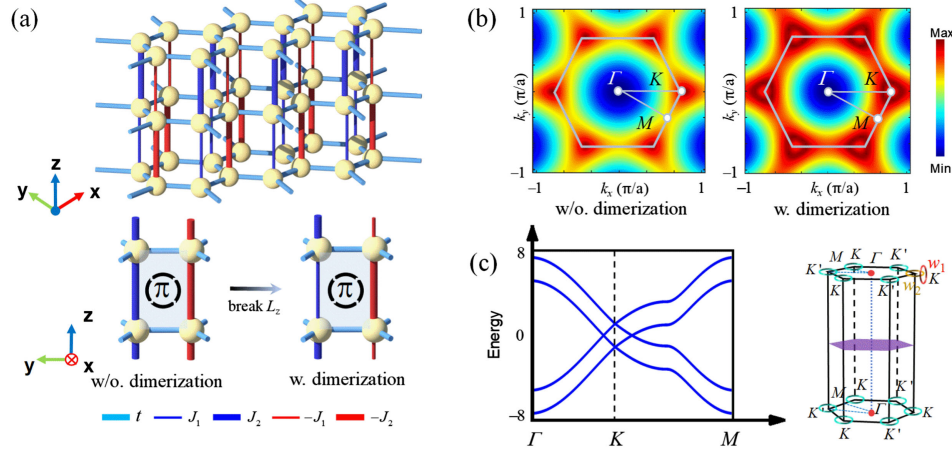


FIG. 1. Tight-binding model of 3D HOTSWS. (a) The schematic of the HOTSWS model, where each unit cell has four sites with different hoppings. The blue and red sticks indicate the positive and negative hoppings, respectively. For the unit cell in the bottom without dimerization, we set  $t = 2.1$ ,  $J_1 = 2.1$ ,  $J_2 = 2.1$ . After breaking  $L_z$ , we obtain the unit cell of HOTSWS, where  $t = 2.1$ ,  $J_1 = 1$ ,  $J_2 = 2.1$ . (b) Evolution process from DPs to nodal loops on the zero-energy surface in  $k$  space. (c) The band structure of HOTSWS along the high-symmetry line of the first BZ. The right panel shows the first BZ where the nodal loops are depicted by cyan rings, and the two Stiefel-Whitney charges of  $w_1$  and  $w_2$  by the perpendicular red and yellow rings.

frequency. The surface and hinge states are demonstrated to selectively distribute on specific surfaces and edges, respectively, which distinguishes the HOTSWS from previous higher-order topological semimetals. Our work reveals that the HOTSWS is a novel higher-order topological phase in  $PT$ -symmetric systems and provides an ideal platform to investigate topological phases of SW classes.

*Construction of the HOTSWS.*—Here, we construct the tight-binding model (TBM) of the HOTSWS in the 3D graphite lattice as depicted in Fig. 1(a). For the single-layer graphene, a double degenerate point appears at  $K$  points in the first Brillouin zone (BZ). By stacking the graphene sonic crystals along the  $z$  direction with alternatively arranged positive and negative couplings of the same strength, we obtain the 3D bilayer graphite with  $\pi$  flux in each plaquette. Thus, the double degenerate Dirac points (DPs) will transform into fourfold degenerate DPs at  $K$  points with  $k_z = \pi$ , where the period along the  $z$  direction is set as one for simplicity. The  $\pi$  flux and related  $\mathbf{Z}_2$  gauge fields redefine the fundamentals of crystal symmetries, which can be deciphered by the Aharonov-Bohm effect. Under  $\mathbf{Z}_2$  gauge field, the lattice translation  $L$  has projective algebraic relations with other spatial symmetries. Hence, the little cogroup at high-symmetry points must contain  $L$  and then the higher-dimensional irreducible representations emerge, which results in the fourfold degenerate DPs at  $K$  points [33]. By breaking the translational symmetry  $L_z$  along the  $z$  direction with dimerized couplings as shown in Fig. 1(a), we can obtain the Hamiltonian kernel of the HOTSWS

$$H_2 = \sigma_0 \otimes H_c + H_z, \quad (1)$$

where  $H_c = \begin{bmatrix} 0 & x_1 \\ x_1^\dagger & 0 \end{bmatrix}$ ,  $H_z = \begin{bmatrix} 0 & H_t \\ H_b & 0 \end{bmatrix}$ ,  $H_t = \begin{bmatrix} J_{13} & 0 \\ 0 & J_{24} \end{bmatrix} = H_b^*$ ,  $x_1 = te^{-i\vec{a}_1 \cdot \vec{k}} + te^{-i\vec{a}_2 \cdot \vec{k}} + te^{-i\vec{a}_3 \cdot \vec{k}}$ ,  $\vec{k} = [k_x, k_y, k_z]$  denotes the wave vector,  $J_{13} = -J_1 - J_2 e^{i\vec{a}_3 \cdot \vec{k}}$ ,  $J_{24} = J_2 + J_1 e^{i\vec{a}_4 \cdot \vec{k}}$ ,  $J_i (i = 1, 2)$  and  $t$  are the interlayer hopping and intralayer hopping amplitudes, respectively. The base vectors of the 3D layered graphite lattice are represented by  $\vec{a}_1$ ,  $\vec{a}_2$ ,  $\vec{a}_3$ , and  $\vec{a}_4$ . To clearly show the evolution process of DP points without and with dimerization, the cross-sectional views of the zero-energy dispersions of our system with  $k_z = \pi$  are displayed in Fig. 1(b). Without dimerization along the  $z$  direction, six highly degenerate DPs emerge at the  $K$  points and evolve into six nodal loops after the dimerization is introduced. This fact can also be verified by the band structure along high-symmetry lines in the first BZ, as shown in Fig. 1(c), where the DPs split into nodal loops. Different from previous higher-order topologies, the HOTSWS is characterized by two distinct topological charges (viz.,  $w_1$  and  $w_2$ ) with real vector bundles, as depicted in the right panel of Fig. 1(c). Paired nodal loops will appear at the corners of the first BZ. The base vectors for calculating  $w_1$  and  $w_2$  in  $k$  space are defined on a circle and a sphere, respectively, and the paired loops enclosed by the circle and sphere carry two topological invariants of SW classes with different topological orders. Here, we schematically represent the SW topological invariants by two crossing rings. In mathematics, the first SW class is an obstruction to the orientability of real bundles over a closed 1D manifold. The 1D manifold is orientable if and only if  $w_1 = 0$ . The second Stiefel-Whitney class is an obstruction to the existence of spin structure on a 2D closed manifold. The spin structure is allowed (or forbidden) when  $w_2 = 0$  (or  $w_2 = 1$ ). Details are explained in the Supplemental

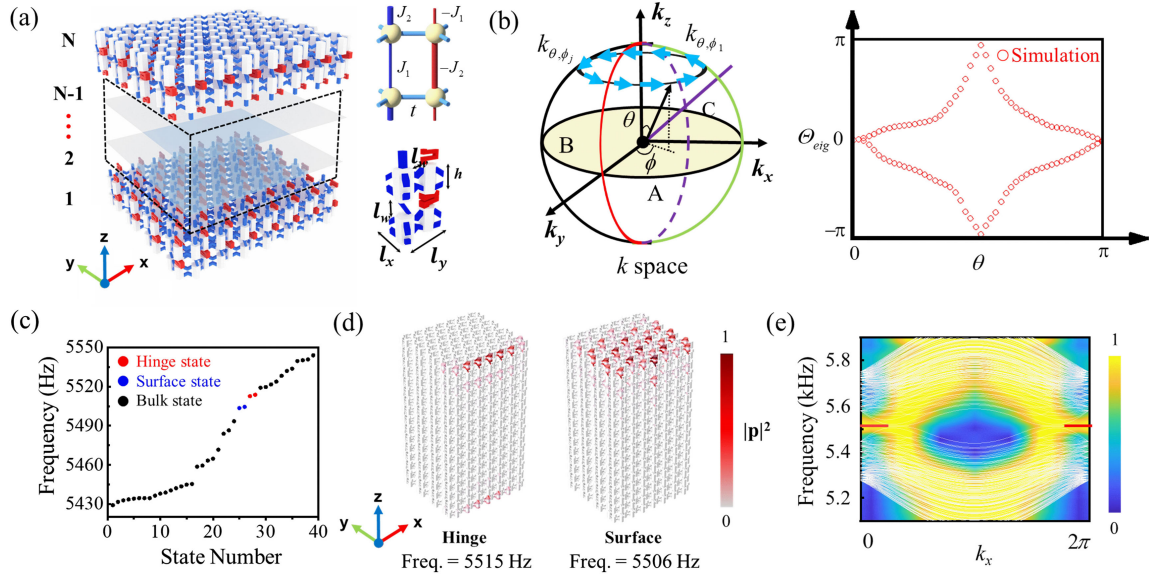


FIG. 2. Acoustic realization of the HOTSWS. (a) A sonic crystal comprising hexagonal acoustic resonators and coupling tubes, in which the blue and red coupling tubes denote the positive and negative couplings, respectively. Up panel inset: the primitive cell of HOTSWS in a toy model. Bottom panel inset: the configuration of one primitive cell in an acoustic system. (b) A sphere centered at  $K$  point in the first BZ, which wraps a nodal loop. The blue arrows ( $N$  wave vectors) mark the circle at a fixed azimuthal angle in  $k$  space. Right panel: Wilson loop spectra. (c) Distribution of eigenstates of HOTSWS. (d) Intensity fields in HOTSWS at 5515 Hz and 5506 Hz, showing the presence of hinge and surface states. (e) The band structure of HOTSWS depicted in white color is calculated from the TBM and the hinge states are marked by the red lines. The thermal diagram shows the dispersion calculated by Fourier transformation from the simulated pressure field.

Material [41]. For the SW classes in physics, the first-order SW invariant  $w_1$  and the second-order SW invariant  $w_2$  correspond to the quantized Berry phase and  $\mathbf{Z}_2$  monopole charge, respectively, where the topological charge  $w_2$  is unique to SW systems [31]. In the BZ, the first SW invariant  $w_1$  is given by

$$w_1 = \frac{1}{\pi} \oint_c dk \cdot \mathbf{A}(\mathbf{k}), \quad (2)$$

where the  $C$  is the closed curve and  $\mathbf{A}(\mathbf{k}) = \langle u_n(\mathbf{k}) | i \nabla_{\mathbf{k}} | u_n(\mathbf{k}) \rangle$  is the Berry connection. The second SW invariant  $w_2$  is given by

$$w_2 = \sum \frac{1}{\pi^2} \oint_{S^2} d\mathbf{S} \cdot \mathbf{A}_n \times \mathbf{A}_m, \quad (3)$$

where  $\mathbf{A}_n/\mathbf{A}_m$  is the Berry connection for the  $n$ th/ $m$ th topmost occupied band and  $S^2$  is a 2D closed manifold in the BZ [31].

*Acoustic realization of the HOTSWS.*—For the acoustic realization of HOTSWS, we employ 3D layered graphite sonic crystal that comprises acoustic resonators and coupling tubes, which are sketched in Fig. 2(a). In principle, we can manipulate the signs and amplitudes of coupling strengths, which are completely determined by the geometries of resonators and tubes. As shown in Fig. 2(a), bilayer-graphene structures are stacked layer by layer in the

$z$  direction, with the inset illustrating the configuration of one unit cell. In the acoustic design of the HOTSWS model, the height and radius of hexagonal cavities in the primitive cell are  $h = 30$  mm and  $R_0 = 10$  mm, the intralayer and interlayer spacings are  $l_w = 16.5$  mm, and the lattice constants in the  $x$  and  $y$  directions are  $l_x = (\sqrt{3}l_w + 3R_0)/2$  mm and  $l_y = (3l_w + 3\sqrt{3}R_0)/2$  mm. The detailed geometric parameters of negative and positive hopping are provided in the Supplemental Material [41]. The couplings of the realistic acoustic model fitted from TBM are as follows  $J_1 \approx 222$  Hz,  $-J_1 \approx -222$  Hz,  $J_2 \approx 461$  Hz,  $-J_2 \approx -461$  Hz,  $t \approx 462$  Hz, and their on-site energy is around 5520 Hz. To quantitatively demonstrate the unique  $w_2$  in acoustic systems, we extract the sound pressure fields corresponding to the discrete points in  $k$  space from a unit cell of acoustic HOTSWS with Bloch-periodic boundaries applied. The spatial bases  $|u_{\theta, \phi_j}\rangle$  are obtained from the one-sphere with a fixed polar angle ( $\theta$ ) as shown in Fig. 2(b). The Wilson loop operator is used in the computation of  $w_2$ , which is defined by

$$W_{(\phi_0+2\pi, \theta) \leftarrow (\phi_0, \theta)} = \lim_{N \rightarrow \infty} F_{N-1} F_{N-2} \dots F_1 F_2, \quad (4)$$

where  $\phi$  and  $\theta$  parametrize a two-sphere, and  $F_j$  is the overlap matrix at  $\phi_j$  with the element  $[F_j]_{mn} = \langle u_{m\phi_{j+1}} | u_{n\phi_j} \rangle$ . We cyclically perform inner products of the basis vectors for energy bands to generate a

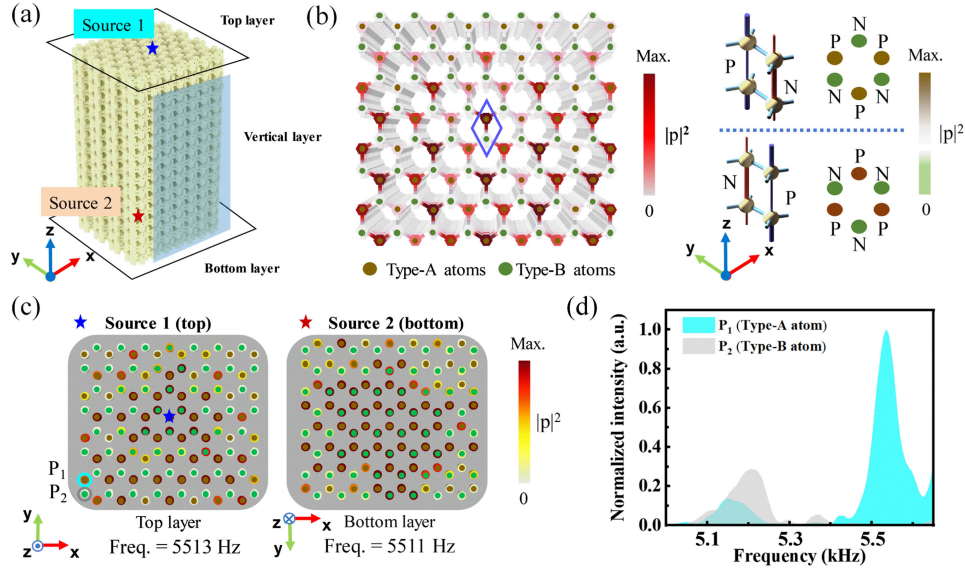


FIG. 3. Surface states in HOTSWS. (a) A schematic of acoustic HOTSWS. The top layer, bottom layer, and vertical layer are highlighted. In experiments, the sources are placed at Source 1 and Source 2 on the top and bottom layer, marked by the blue and red stars, aiming at exciting the surface states. (b) The distribution of surface states on the top layer, where acoustic intensity fields are majorly localized at the sites of Type-A atoms. The blue box covers a unit cell of HOTSWS, in which the Type-A and Type-B atoms are denoted by brown and green dots. The right panel shows the acoustic intensity in one unit cell, where acoustic fields are localized in the cavities connected with positive interlayer couplings. (c) The measured intensity field distributions on the top and bottom layers. (d) The transmission spectra measured at Ports  $P_1$  and  $P_2$ , marked by the blue and gray circles in (c).

non-Abelian matrix  $M_{\theta,\phi}$ . Then, we multiply  $M_{\theta,\phi}$  cumulatively to obtain  $W_\theta$  as

$$W_\theta = \prod_{\phi=1}^N M_{\theta,\phi}, \quad (5)$$

where the eigenvalue of  $W_\theta$  is  $w_\theta$  and  $\Theta = i \log(w_\theta)$ . As shown in the right panel of Fig. 2(b), the second-order SW invariant  $w_2$  can be obtained from the parity of number of Wilson loop spectra linearly crossing on  $\Theta_{\text{eig}} = \pi$ , and  $w_2 = 1$  in our design [31].

Then, we numerically calculate the eigenfrequencies of the sonic crystal in Fig. 2(c). The red and blue dots represent the hinge and surface modes of HOTSWS, which slightly split in frequencies due to the finite-size effect. The intensity fields of the hinge and surface modes in acoustic HOTSWS are displayed in Fig. 2(d). In the simulation, the source is placed at the center of the top layer. By extracting pressure fields on the hinge of the top layer and performing Fourier transformation, we further simulate the dispersions of the hinge and bulk states, which are shown in the thermal diagrams, in good agreement with the hinge states (red-colored lines) and bulk states (white-colored lines) from the tight-binding calculation, as shown in Fig. 2(e).

*Surface states in the HOTSWS.*—We utilize 3D printing technology to fabricate the sample of acoustic HOTSWS. In Fig. 3(a), the 3D structure has  $7 \times 7 \times 8$  unit cells, containing 1920 acoustic resonators. For the resonators on

the top and bottom layers, a hole is perforated in each resonator for inserting a source or a probe. Two sources (Source 1 and Source 2), denoted by the blue and red stars on the top and bottom layers, are used for the excitation of surface states. In Fig. 3(b), we show the simulated intensity field distribution of surface states on the top layer, where the energy is mostly localized in the cavities (brown dot) corresponding to the Type-A atoms. However, in the cavities (green dot) corresponding to Type-B atoms, acoustic energy is not localized. The right panel of Fig. 3(b) shows the field polarization for the surface states. Specifically, the field localization depends on the sign of interlayer couplings (positive hopping: P, negative hopping: N). Therefore, when we swap the P and N interlayer couplings, the surface-state field distribution will change accordingly. Note that the field distribution is not homogenous on the top surface and is always inclined to accumulate toward the boundary connected with positive interlayer couplings. We experimentally measure the acoustic intensity fields of surface states in Fig. 3(c). The results demonstrate that the surface states on the top and bottom layers do exist, where the energies of surface states are selectively localized in the cavities corresponding to Type-A atoms. Our experimental result agrees well with the simulation. To illustrate the field polarization, we show the transmission spectra at the Ports  $P_1$  (Type-A atom) and  $P_2$  (Type-B atom) in Fig. 3(d), for which  $P_1$  and  $P_2$  are marked by the blue and gray circles in Fig. 3(c). At the frequency where surface states exist, the sound intensity at Port  $P_1$  is much larger than the one at

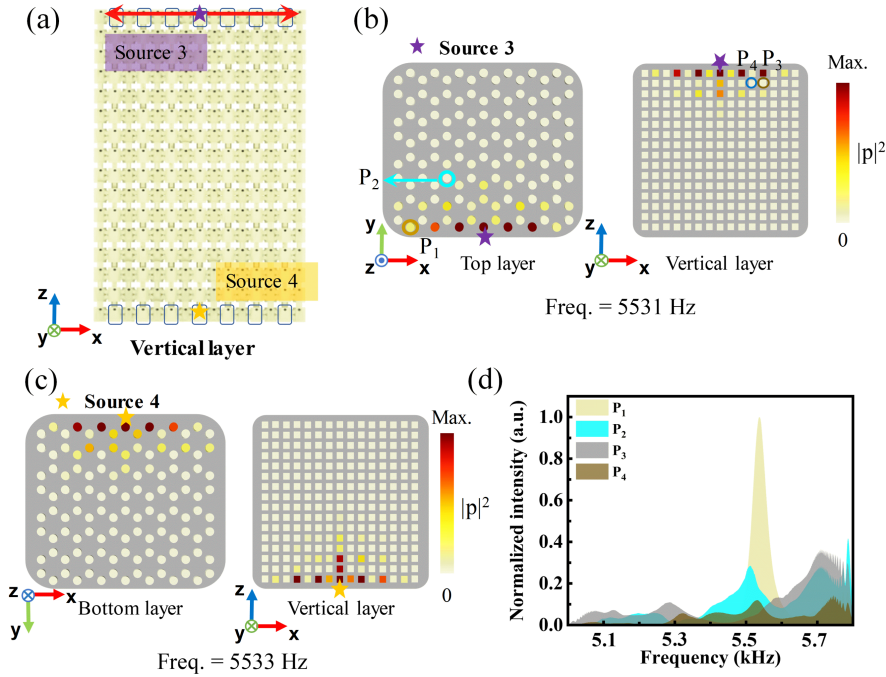


FIG. 4. Hinge states in HOTSWS. (a) The section in the  $x - z$  plane of the sample. Locations of the sound sources (Source 3 and Source 4) are marked by the purple and yellow stars, respectively. (b),(c) Measured acoustic intensity field distributions for the hinge states when the sources are placed on the (b) top layer (Source 3) and (c) bottom layer (Source 4). (d) The transmission spectra measured at the Ports  $P_1$ ,  $P_2$ ,  $P_3$  (Type-A atom), and  $P_4$  (Type-B atom) marked by the circles in (b), reveal the properties of hinge states, surface states, and bulk states in the frequency domain.

Port  $P_2$ , while the intensities at Ports  $P_1$  and  $P_2$  are close to each other at other frequencies.

*Hinge states in the HOTSWS.*—As mentioned, the surface states protected by the first-order topological charge  $w_1$  have the same frequency as the hinge states protected by the second-order topological charge  $w_2$ . Here, we experimentally visualize the hinge states in the acoustic HOTSWS sample. In Fig. 4(a), we show the  $x - z$  plane section of the acoustic sample, where the excitation is set at Source 3 and Source 4, respectively, to excite the hinge states on the top and bottom layers of HOTSWS. The measured intensity field distributions of hinge states are shown in Figs. 4(b) and 4(c), which are featured with the field localization at the specific edges in pairs. To compare the transport properties of the hinge states, surface states, and bulk states in acoustic HOTSWS, we further measure transmission spectra at Ports  $P_1$ ,  $P_2$ ,  $P_3$ , and  $P_4$ , as shown in Fig. 4(d). The spectra for hinge states and surface states have two prominent peaks at 5531 Hz and 5511 Hz, which correspond to  $P_1$  and  $P_2$ , where the  $Q$  factor for the hinge states reaches up to  $\sim 118$ . The transmission spectra for the bulk states at  $P_3$  and  $P_4$  indicate severe sound diffusion, compared with those of the hinge and surface states. Note that the peaks for hinge and surface states differ slightly in the spectrum (about 20 Hz). More details of the experiments are provided in Supplemental Material [41].

*Conclusion and outlook.*—We have demonstrated a novel higher-order topological phase of reciprocal and

spinless SW topological semimetal, which has two different bulk-boundary correspondences characterized by two SW topological invariants. SW topological semimetal differs from the previously identified topological semimetals associated with the Chern classes, while its corresponding SW classes are as important as the Chern classes in the mathematical framework. In this work, we have obtained the SW class topological invariants by extracting the pressure field in an acoustic HOTSWS lattice. The topological hinge and surface states in HOTSWS have been experimentally measured, visualized, and spotted around the same frequency. HOTSWSs with the properties of stable nodal loops and selective distributions of the localized energy may have potential applications in topological sensing and trapping, and they can also be readily realized in other systems, including photonics and topoelectrical circuits to further promote the exploration of SW class physics.

We thank Zhe-Qi Wang and Professor Zhen Huan from Huazhong University of Science and Technology and Professor Rui Yu from Wuhan University for their helpful discussions. The authors acknowledge financial support by the National Natural Science Foundation of China (Grant No. 12304492), X. N. acknowledges the support from the Research Startup Fund of Central South University (Grant No. 11400-506030109).

\*Corresponding author: ygpeng@hust.edu.cn

†Corresponding author: nixiang@csu.edu.cn

‡Corresponding author: xfzhu@hust.edu.cn

- [1] J. E. Moore, The birth of topological insulators, *Nature (London)* **464**, 194 (2010).
- [2] M. Z. Hasan and C. L. Kane, Colloquium: Topological insulators, *Rev. Mod. Phys.* **82**, 3045 (2010).
- [3] X.-L. Qi and S.-C. Zhang, Topological insulators and superconductors, *Rev. Mod. Phys.* **83**, 1057 (2011).
- [4] F. D. M. Haldane, Model for a quantum Hall effect without Landau levels: Condensed-matter realization of the “parity anomaly”, *Phys. Rev. Lett.* **61**, 2015 (1988).
- [5] C. L. Kane and E. J. Mele, Z(2) topological order and the quantum spin Hall effect, *Phys. Rev. Lett.* **95**, 146802 (2005).
- [6] C. L. Kane and E. J. Mele, Quantum spin Hall effect in graphene, *Phys. Rev. Lett.* **95**, 226801 (2005).
- [7] B. A. Bernevig and S.-C. Zhang, Quantum spin Hall effect, *Phys. Rev. Lett.* **96**, 106802 (2006).
- [8] A. G. Grushin, A. Gomez-Leon, and T. Neupert, Floquet fractional Chern insulators, *Phys. Rev. Lett.* **112**, 156801 (2014).
- [9] J. Y. Lu, C. Y. Qiu, M. Z. Ke, and Z. Y. Liu, Valley vortex states in sonic crystals, *Phys. Rev. Lett.* **116**, 093901 (2016).
- [10] Y. J. Ding, Y. G. Peng, Y. F. Zhu, X. D. Fan, J. Yang, B. Liang, X. F. Zhu, X. G. Wan, and J. C. Cheng, Experimental demonstration of acoustic Chern insulators, *Phys. Rev. Lett.* **122**, 014302 (2019).
- [11] T. Ozawa, H. M. Price, A. Amo, N. Goldman, M. Hafezi, L. Lu, M. C. Rechtsman, D. Schuster, J. Simon, O. Zilberberg, and I. Carusotto, Topological photonics, *Rev. Mod. Phys.* **91**, 015006 (2019).
- [12] H. Xue, Y. Yang, and B. Zhang, Topological acoustics, *Nat. Rev. Mater.* **7**, 974 (2022).
- [13] C. W. Peterson, W. A. Benalcazar, T. L. Hughes, and G. Bahl, A quantized microwave quadrupole insulator with topologically protected corner states, *Nature (London)* **555**, 346 (2018).
- [14] M. Serra-Garcia, V. Peri, R. Süsstrunk, O. R. Bilal, T. Larsen, L. G. Villanueva, and S. D. Huber, Observation of a phononic quadrupole topological insulator, *Nature (London)* **555**, 342 (2018).
- [15] X. Ni, M. Weiner, A. Alu, and A. B. Khanikaev, Observation of higher-order topological acoustic states protected by generalized chiral symmetry, *Nat. Mater.* **18**, 113 (2019).
- [16] H. Xue, Y. Yang, F. Gao, Y. Chong, and B. Zhang, Acoustic higher-order topological insulator on a kagome lattice, *Nat. Mater.* **18**, 108 (2019).
- [17] X. Ni, M. Y. Li, M. Weiner, A. Alu, and A. B. Khanikaev, Demonstration of a quantized acoustic octupole topological insulator, *Nat. Commun.* **11**, 2108 (2020).
- [18] Y. J. Qi, C. Y. Qiu, M. Xiao, H. L. He, M. Z. Ke, and Z. Y. Liu, Acoustic realization of quadrupole topological insulators, *Phys. Rev. Lett.* **124**, 206601 (2020).
- [19] Z.-G. Chen, W. Zhu, Y. Tan, L. Wang, and G. Ma, Acoustic realization of a four-dimensional higher-order Chern insulator and boundary-modes engineering, *Phys. Rev. X* **11**, 011016 (2021).
- [20] Z. Song, Z. Fang, and C. Fang, (d-2)-dimensional edge states of rotation symmetry protected topological states, *Phys. Rev. Lett.* **119**, 246402 (2017).
- [21] M. Ezawa, Higher-order topological insulators and semimetals on the breathing kagome and pyrochlore lattices, *Phys. Rev. Lett.* **120**, 026801 (2018).
- [22] F. Schindler, A. M. Cook, M. G. Vergniory, Z. Wang, S. S. Parkin, B. A. Bernevig, and T. Neupert, Higher-order topological insulators, *Sci. Adv.* **4**, eaat0346 (2018).
- [23] Sayed Ali Akbar Ghorashi, T. Li, and T. L. Hughes, Higher-order Weyl semimetals, *Phys. Rev. Lett.* **125**, 266804 (2020).
- [24] H.-X. Wang, Z.-K. Lin, B. Jiang, G.-Y. Guo, and J.-H. Jiang, Higher-order Weyl semimetals, *Phys. Rev. Lett.* **125**, 146401 (2020).
- [25] M. Weiner, X. Ni, M. Li, A. Alù, and A. B. Khanikaev, Demonstration of a third-order hierarchy of topological states in a three-dimensional acoustic metamaterial, *Sci. Adv.* **6**, eaay4166 (2020).
- [26] H. Gao, H. Xue, Z. Gu, T. Liu, J. Zhu, and B. Zhang, Non-Hermitian route to higher-order topology in an acoustic crystal, *Nat. Commun.* **12**, 1888 (2021).
- [27] L. Luo, H. X. Wang, Z. K. Lin, B. Jiang, Y. Wu, F. Li, and J. H. Jiang, Observation of a phononic higher-order Weyl semimetal, *Nat. Mater.* **20**, 794 (2021).
- [28] Q. Wei, X. Zhang, W. Deng, J. Lu, X. Huang, M. Yan, G. Chen, Z. Liu, and S. Jia, Higher-order topological semimetal in acoustic crystals, *Nat. Mater.* **20**, 812 (2021).
- [29] Q. Wei, X. Zhang, W. Deng, J. Lu, X. Huang, M. Yan, G. Chen, Z. Liu, and S. Jia, 3D hinge transport in acoustic higher-order topological insulators, *Phys. Rev. Lett.* **127**, 255501 (2021).
- [30] Z. Pu, H. He, L. Luo, Q. Ma, L. Ye, M. Ke, and Z. Liu, Acoustic higher-order Weyl semimetal with bound hinge states in the continuum, *Phys. Rev. Lett.* **130**, 116103 (2023).
- [31] J. Ahn, D. Kim, Y. Kim, and B.-J. Yang, Band topology and linking structure of nodal line semimetals with  $Z_2$  monopole charges, *Phys. Rev. Lett.* **121**, 106403 (2018).
- [32] Z. Wang, B. J. Wieder, J. Li, B. Yan, and B. A. Bernevig, Higher-order topology, monopole nodal lines, and the origin of large Fermi arcs in transition metal dichalcogenides  $XTe_2$  ( $X = Mo, W$ ), *Phys. Rev. Lett.* **123**, 186401 (2019).
- [33] L. B. Shao, Q. Liu, R. Xiao, S. Y. A. Yang, and Y. X. Zhao, Gauge-field extended  $k \cdot p$  method and novel topological phases, *Phys. Rev. Lett.* **127**, 076401 (2021).
- [34] Y. X. Huang, Z. Y. Chen, X. Feng, S. A. Yang, and Y. X. Zhao, Periodic Clifford symmetry algebras on flux lattices, *Phys. Rev. B* **106**, 125102 (2022).
- [35] C. Chen, X. T. Zeng, Z. Y. Chen, Y. X. Zhao, X. L. Sheng, and S. A. Yang, Second-order real nodal-line semimetal in three-dimensional graphdiyne, *Phys. Rev. Lett.* **128**, 026405 (2022).
- [36] A. Hatcher, *Algebraic Topology* (Cambridge University, Cambridge, England, 2002).
- [37] T. Li, J. Du, Q. Zhang, Y. Li, X. Fan, F. Zhang, and C. Qiu, Acoustic mobius insulators from projective symmetry, *Phys. Rev. Lett.* **128**, 116803 (2022).
- [38] H. Xue, Z. Wang, Y.-X. Huang, Z. Cheng, L. Yu, Y. X. Foo, Y. X. Zhao, S. A. Yang, and B. Zhang, Projectively enriched symmetry and topology in acoustic crystals, *Phys. Rev. Lett.* **128**, 116802 (2022).

- [39] T. Z. Li, L. H. Liu, Q. C. Zhang, and C. Y. Qiu, Acoustic realization of projective mirror Chern insulators, *Commun. Phys.* **6**, 268 (2023).
- [40] Y. Meng, S. Lin, B. J. Shi, B. Wei, L. Yang *et al.*, Spinful topological phases in acoustic crystals with projective PT symmetry, *Phys. Rev. Lett.* **130**, 026101 (2023).
- [41] See Supplemental Material at <http://link.aps.org/supplemental/10.1103/PhysRevLett.132.197202> for theoretical details of SW classes, numerical and experimental details, and the advantages of different platforms, which includes Refs. [31–36,42–65].
- [42] M. Nakahara, *Geometry, Topology and Physics*, 2nd ed. (CRC Press, Taylor & Francis Ltd, Boca Raton, Florida, 2003).
- [43] J. Ahn, S. Park, D. Kim, Y. Kim, and B.-J. Yang, Stiefel–Whitney classes and topological phases in band theory, *Chin. Phys. B* **28**, 117101 (2019).
- [44] C. H. Lee, S. Imhof, C. Berger, F. Bayer, J. Brehm, L. W. Molenkamp, T. Kiessling, and R. Thomale, Topolectrical circuits, *Commun. Phys.* **1**, 39 (2018).
- [45] J. Dong, V. Juričić, and B. Roy, Topolectric circuits: Theory and construction, *Phys. Rev. Res.* **3**, 023056 (2021).
- [46] T. Helbig, T. Hofmann, S. Imhof, M. Abdelghany, T. Kiessling, L. W. Molenkamp, C. H. Lee, A. Szameit, M. Greiter, and R. Thomale, Generalized bulk–boundary correspondence in non-Hermitian topolectrical circuits, *Nat. Phys.* **16**, 747 (2020).
- [47] D. Zou, T. Chen, W. He, J. Bao, C. H. Lee, H. Sun, and X. Zhang, Observation of hybrid higher-order skin-topological effect in non-Hermitian topolectrical circuits, *Nat. Commun.* **12**, 7201 (2021).
- [48] S. Liu, S. Ma, C. Yang, L. Zhang, W. Gao, Y. J. Xiang, T. J. Cui, and S. Zhang, Gain-and loss-induced topological insulating phase in a non-Hermitian electrical circuit, *Phys. Rev. Appl.* **13**, 014047 (2020).
- [49] W. Rui, Y. Zhao, and Z. Wang, Making topologically trivial non-Hermitian systems nontrivial via gauge fields, *Phys. Rev. Lett.* **131**, 176402 (2023).
- [50] W. Zhang, D. Zou, J. Bao, W. He, Q. Pei, H. Sun, and X. Zhang, Topolectrical-circuit realization of a four-dimensional hexadecapole insulator, *Phys. Rev. B* **102**, 100102(R) (2020).
- [51] Y. Wang, H. M. Price, B. Zhang, and Y. Chong, Circuit implementation of a four-dimensional topological insulator, *Nat. Commun.* **11**, 2356 (2020).
- [52] X. Zheng, T. Chen, and X. Zhang, Topological states in a five-dimensional non-Hermitian system, *Phys. Rev. B* **109**, 085307 (2024).
- [53] F. Gao, X. Xiang, Y.-G. Peng, X. Ni, Q.-L. Sun, S. Yves, X.-F. Zhu, and A. Alù, Orbital topological edge states and phase transitions in one-dimensional acoustic resonator chains, *Nat. Commun.* **14**, 8162 (2023).
- [54] F. Gao, Y. G. Peng, X. Xiang, X. Ni, C. Zheng, S. Yves, X. F. Zhu, and A. Alù, Acoustic higher-order topological insulators induced by orbital-interactions, *Adv. Mater.* **2312421** (2024).
- [55] F. Gao, Y.-G. Peng, Q.-L. Sun, X. Xiang, C. Zheng, and X.-F. Zhu, Topological acoustics with orbital-dependent gauge fields, *Phys. Rev. Appl.* **20**, 064036 (2023).
- [56] J. Yao, X. Hao, B. Song, Y. Jia, C. Hua, and M. Zhou, Multi-orbital topolectrical circuit for topological quantum states, *Nano Futures* **6**, 021001 (2022).
- [57] Y. Makhlin, G. Schön, and A. Shnirman, Quantum-state engineering with Josephson-junction devices, *Rev. Mod. Phys.* **73**, 357 (2001).
- [58] M. Mariani *et al.*, Implementing the quantum von Neumann architecture with superconducting circuits, *Science* **334**, 61 (2011).
- [59] F. Arute *et al.*, Quantum supremacy using a programmable superconducting processor, *Nature (London)* **574**, 505 (2019).
- [60] J. Koch, T. M. Yu, J. Gambetta, A. A. Houck, D. I. Schuster, J. Majer, A. Blais, M. H. Devoret, S. M. Girvin, and R. J. Schoelkopf, Charge-insensitive qubit design derived from the Cooper pair box, *Phys. Rev. A* **76**, 042319 (2007).
- [61] R. Barends *et al.*, Superconducting quantum circuits at the surface code threshold for fault tolerance, *Nature (London)* **508**, 500 (2014).
- [62] D. L. Underwood, W. E. Shanks, J. Koch, and A. A. Houck, Low-disorder microwave cavity lattices for quantum simulation with photons, *Phys. Rev. A* **86**, 023837 (2012).
- [63] C. Song *et al.*, Demonstration of topological robustness of anyonic braiding statistics with a superconducting quantum circuit, *Phys. Rev. Lett.* **121**, 030502 (2018).
- [64] X. Tan, Y. Zhao, Q. Liu, G. Xue, H.-F. Yu, Z. Wang, and Y. Yu, Simulation and manipulation of tunable Weyl-semimetal bands using superconducting quantum circuits, *Phys. Rev. Lett.* **122**, 010501 (2019).
- [65] Z.-C. Xiang *et al.*, Simulating Chern insulators on a superconducting quantum processor, *Nat. Commun.* **14**, 5433 (2023).